Physicochem. Probl. Miner. Process., 61(6), 2025, 215664

http://www.journalssystem.com/ppmp

Physicochemical Problems of Mineral Processing

ISSN 1643-1049

Research of fluid-particle passing through screen in multi-stage hydrocyclone–screen model based on CFD-DEM algorithms

Chuanzhen Wang [1], Tao Tan [1], Min Li [1], Andile Khumalo [1], Fengcheng Jiang [1], Md. Shakhaoath Khan [2]

[1] Anhui Engineering Research Center for Coal Clean Processing and Carbon Reduction, College of Material Science and Engineering, Anhui University of Science and Technology, Huainan 232001

[2] Department of Chemical Engineering, Monash University, Clayton, VIC 3800, Australia

Corresponding author: faxofking@cumt.edu.cn (Chuanzhen Wang)

Abstract: A novel three-product hydrocyclone screening device (TPHS) has been successfully developed. Through systematic research and experimentation, this equipment demonstrates superior efficiency and throughput compared to conventional hydrocyclones in coal slurry classification. While improvements in classification efficiency and processing capacity have been achieved, insufficient exploration exists regarding the unique screening-through classification zone. Therefore, this paper establishes a multi-stage hydrocyclone screening-through model (MHS) to investigate its flow field and classification characteristics. This study employs Fluent and CFD-DEM simulations to investigate the swirl flow field characteristics, examining the flow patterns within the cyclone screening structure and its impact on particle motion. Results indicate: - High turbulence intensity and uneven velocity distribution in the first flow channel significantly affect fluid velocities within the cyclone tube. Complex turbulence within the first screen aperture affects subsequent particle screening, prolonging the screening process. At a rotational radius R=75, radial forces dominate the flow field, facilitating particle screening in the separation zone. Under vortex influence, particles exhibit three distinct motion trajectories within the screening region.

***Keywords*:** three-product hydrocyclone screening device, hydrocyclones, multi-stage hydrocyclone screening-through model, CFD-DEM

1. Introduction

The hydrocyclone is a device that utilizes centrifugal force to separate immiscible gases and liquids, accelerating the sedimentation of mineral particles to achieve particle size classification. Hydraulic cyclones offer advantages such as compact size (Al Kayed Quteishat, 2020), simple structure (Li, et al., 2020), ease of maintenance (Bing, et al., 2020), and high classification efficiency (Salvador, et al., 2016). Consequently, they find extensive application across numerous sectors, including petroleum, biotechnology (Ji, et al., 2023), metallurgy (Padhi, et al., 2022), and rare earth recovery (Yu, et al., 2017). However, as industrial production precision continues to rise, traditional hydraulic cyclones exhibit certain limitations. Current engineering applications demand increasingly higher performance from these devices, with structural improvements emerging as a key approach to enhancing their capabilities (Jung, et al., 2019). Numerical simulation serves as an effective means to reduce the experimental costs associated with structural optimization of hydrocyclones. The rapid advancement of Computational Fluid Dynamics (CFD) and the Discrete Element Method (DEM) has propelled the application of CFD-DEM coupled computations across multiple fields (Kuang, et al., 2020; Zhang, et al., 2019), including chemistry (Yu, et al., 2023) and biology (El-Emam, et al., 2021). Consequently, the CFD-DEM coupling (Kuruneru, et al., 2018) approach has also emerged as an effective pathway for investigating hydrocyclones (Chu, et al., 2017; Fulchini, et al., 2019) and exploring anomalous particle behaviour and macroscopic characteristics (Gao, et al., 2023; Esgandari, et al., 2021).

The internal structural characteristics of hydrocyclones have been extensively investigated and modified through multifaceted research by scholars. To optimise hydrocyclone classification

DOI: 10.37190/ppmp/215664

performance, Li et al (2018) and Zhang et al (2021). modified the structure of conventional hydrocyclones to alter their internal flow fields. Numerical simulations of the separation mechanisms under various structures demonstrated that the separation efficiency and precision of hydrocyclones with modified structures were enhanced. C.A.O. Rocha et al (Rocha, et al., 2020). comparatively analysed the impact of circular versus square feed pipes on hydrocyclone separation performance. Findings indicated that square feed pipes, compared to circular ones, increased the hydrocyclone's Euler number and the ratio of underflow to feed volume, with the square cross-section enhancing classification capability. Hou, et al. (2022) proposed three novel hydrocyclone designs based on the traditional cylindrical-conical and cylindrical configurations. Numerical simulations revealed that at high tangential velocities, the MS-type (multi-stage cylindrical) design enhances internal swirl and axial circulation, thereby reducing misclassification of fine particles. We have thus designed a three products hydrocyclone screen (TPHS) and conducted systematic research (Wang, et al., 2020) and experiments (Li, et al.,2011; Zhang, et al., 2011; Chen, et al., 2016). To further investigate the internal flow field and particle characteristics within the TPHS, a CFD-DEM coupled calculation was employed to analyse these aspects.

Exploratory work conducted on the TPHS has yielded significant results. While previous research primarily focused on the equipment collectively, insufficient attention has been paid to the unique screening and grading zones. This paper therefore addresses this knowledge gap by employing particle image velocimetry (PIV) and CFD-DEM methodologies to conduct an in-depth investigation of the screening zones within the cyclone screening structure, and the objectives of the current work are as follows:

(1) Verification of the correctness of the Multi-stage Hydrocyclone - Screen structure model by comparing the results of PIV experiments with CFD simulation experiments.

(2) The results of the numerical analysis are utilized to fully characterize the internal flow field of the Multi-stage Hydrocyclone - Screen structure including the velocity vector direction and distribution.

(3) The results of the coupled CFD-DEM simulation are utilized to describe the internal particle motion characteristics of the Multi-stage Hydrocyclone - Screen structure, including velocity changes, velocity distributions, and motion trajectories.

2. Materials and methods

2.1. Experimental

Fig. 1 presents photographs of the PIV experimental setup (a) and schematic diagram (b). The experiment comprises two subsystems: a flow field operation platform and a PIV detection system. The flow field operation platform generates a co-rotating flow field via a Multi-stage Hydrocyclone - Screen structure (MHS). A variable-speed pump (driven by a 0.37kW three-phase asynchronous motor) regulates flow rate, which is measured by an ultrasonic flowmeter and monitored by a pressure gauge. The Multi-stage Hydrocyclone - Screen structure (MHS) is enclosed within a water-filled cubic housing to eliminate light refraction. Both the housing and structure are fabricated from optically transparent PMMA material. The PIV detection system comprises a dual-pulse laser, CCD camera, synchronization controller, and workstation. The laser emits a horizontal beam illuminating 10-micron fluorescent polymer tracer particles within the flow field. These particles, carried by fluid motion, are captured by the CCD camera. The synchronization controller ensures precise alignment between laser emission and camera imaging, enabling accurate capture of the flow field velocity distribution.

Step 1 Position the subsystem under test at the inspection point, ensuring it remains parallel to the PIV system. Maintain 25–40 cm distance between the cube enclosure housing the swirl-flow separation structure and the dual-pulse laser. Then activate the continuous laser, reduce its intensity, and adjust its height to ensure the laser beam covers the entire observation area. Next, position the industrial camera directly above the observation area. Finally, slowly fill the cube enclosure with deionized water at 40–50°C using the siphon method, avoiding air bubbles to ensure observation accuracy.

Step 2 Fill the feed tank approximately two-thirds full with deionized water. Start the variable-frequency water pump at a low frequency of 10 Hz. Once operation stabilizes, gradually increase the frequency to ensure water fills the flow channels and expels all air bubbles. After approximately 10 minutes of operation, replenish the deionized water to the original level. Add an appropriate amount

of tracer particles, stir with an acrylic rod for 5 minutes, and continue operation for another 10 minutes to ensure uniform particle distribution. Adjust the camera position and focal length using Dynamic Studio software, then perform calibration. After installing the filter, darken the environment to a darkroom state. Turn on the laser and gradually increase the laser intensity to a safe level where particle brightness is optimal. Finally, capture and save the images.

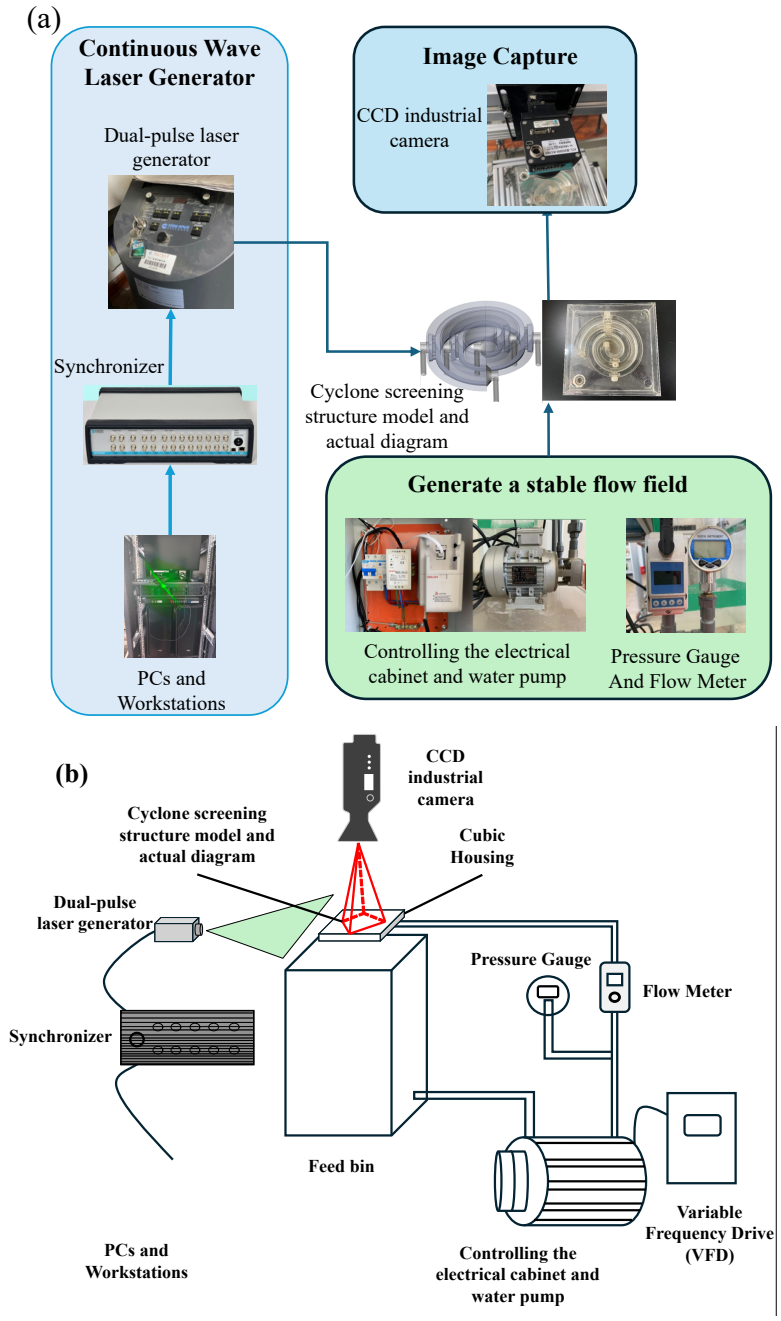

Fig. 1. PIV Experimental setup: (a) Setup diagram, (b) Schematic diagram

Step 3 Process the acquired images by first applying Dynamic Studio's Top-hat morphological filter for noise reduction, then using Region of Interest ROI Extract to select the rectangular regions requiring analysis. Subsequently, employ an adaptive cross-correlation algorithm to compute the instantaneous velocity field based on the displacement of tracer particles across two image frames. Verify dispersion ranges to remove anomalous velocity vectors and compensate with neighboring data to minimize computational errors. Subsequently, the Average filter algorithm is applied to smooth the data within a 3×3-pixel range. Finally, the instantaneous velocity fields from 200 different time points are averaged to obtain the time-averaged velocity distribution map.

2.2. Numerical models

2.2.1. Model structure

The study focused on the classification process and flow field within the TPHS screen gap region. The experimental design involved systematically replacing the TPHS with units of different cyclone radii to isolate their effect. Therefore, a novel cyclone classification structure, namely Multi-stage Hydrocyclone - Screen Mesh model (MHS), is proposed, as shown in Fig. 2. This model comprises four vortex tubes with distinct rotational radii: 18.75 mm, 37.5 mm, 56.25 mm, and 75 mm. Three screen apertures are positioned at the mid-sections of each vortex tube, with the regions outside these apertures connected to the outlet. The model features one inlet and five outlets. The inlet is positioned at the initial end of the 18.75 mm radius tube, while the outlets are located at the mid-sections of the four vortex tubes and at the end of the 75 mm radius vortex tube. Detailed model parameters are listed in Table 1.

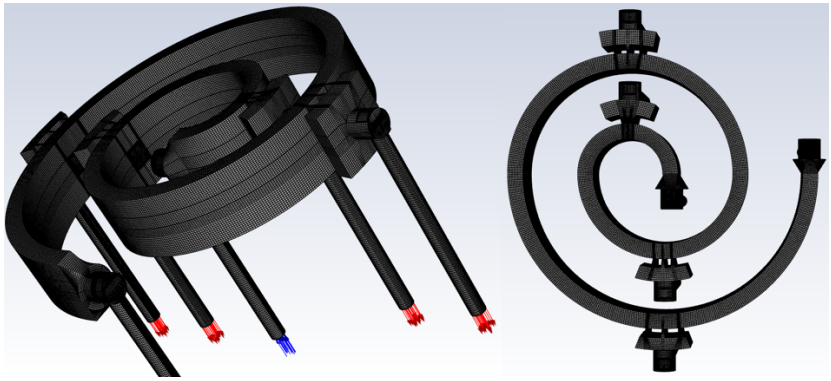

Fig. 2. Multi-stage hydrocyclone - screen mesh structure model

Table 1. Multi-stage hydrocyclone - screen mesh structural parameters

Items	Geometric parameters
First segment radius of rotation	18.75mm
Second segment radius of rotation	37.5mm
Third segment radius of rotation	56.25mm
Fourth segment radius of rotation	75mm
Swirl duct length x width	30mm×8mm
Cuboid casing length x width	250mm×250mm
Inlet diameter	7mm
Outlet diameter	7mm
Narrow end width of screen opening	0.66mm
Screen slot width at the wide end	2mm
The length of the screen gap	5mm

To further investigate the motion characteristics of particles within the cyclonic screening structure, the first section of the integrated model was selected as the subject of study, with its schematic structure shown in Fig. 3. A CFD-DEM coupled approach was employed to numerically simulate the flow and particle behaviour within this region. This model was extracted from the integrated model at a rotational radius of R = 18.75 mm, with parameters such as screen aperture size, height, and aperture length maintained consistent with the integrated model. Specific parameters are detailed in Table 1.

2.2.2. Multi-phase flow models

Within the cyclone screening structure, the predominant phases are gas-liquid two-phase flow, where water constitutes the primary phase and air the secondary phase. The Volume of Fluid VOF model tracks different phase interfaces by solving the continuity equation for the volume fraction of one or

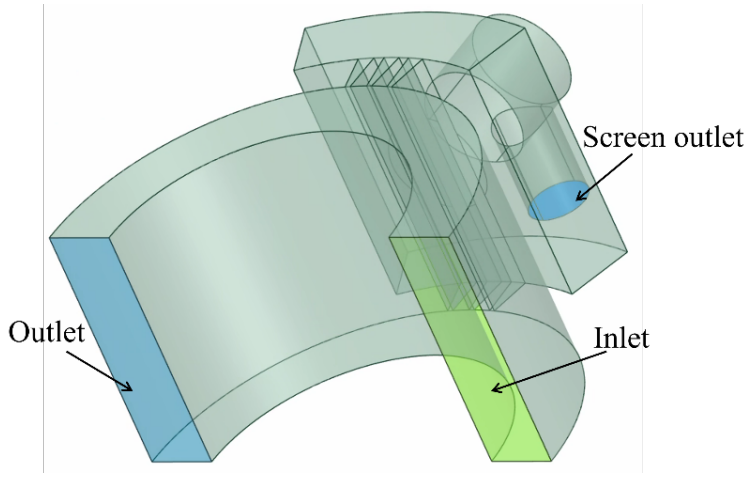

Fig. 3. hydrocyclone - screen structure model

more phases (Mulbah, et al., 2022). This model proves highly advantageous for investigating the transient flow characteristics of fluids during cyclone screening.

Kopparthy et al (2020). compared four turbulence models with detailed experimental data in their study of diffusers, finding that the RSM performed better in predicting the experimental velocity field and flow pattern aggregation. Zhipeng Xiong et al (Xiong, et al., 2023). obtained separation efficiencies from RSM simulations that matched experimental data, demonstrating that the RSM model can provide reasonable and reliable predictions for the hydraulic behaviour and separation performance of hydrocyclones. In Vysyaraju et al. (2022)'s novel hydrocyclone design, the LES-WALE model demonstrated superior agreement with experimental observations compared to other turbulence models, despite its substantial computational time requirements. Misiulia et al. (2021). observed in cyclone separator studies that employing the LES model for the continuous phase yielded optimal results. These relevant studies indicate that each turbulence model possesses certain modelling capabilities. Consequently, selecting an appropriate turbulence model based on the complexity of the MHS, computational time, and available computational resources is of paramount importance (Vakamalla and Mangadoddy, 2017). The equations used in the flow field are shown in Table 2.

Table 2. Formula in the flow field

Items	Models	
VOF equation:	$\frac{1}{\rho_q}\left[\frac{\hat{c}}{ct}(\alpha_q\rho_q)+\nabla\cdot\left(\alpha_q\rho_q\overset{\Gamma}{u}_q\right)=\sum_{p=1}^{n}\left(\dot{m}_{pq}-\dot{m}_{qp}\right)\right]$	(1)
Continuity equation:	$\frac{\partial\rho}{\partial t}+\frac{\partial\rho}{\partial x_i}(\rho u_i)=0$	(2)
Motion equation:	$\frac{\partial}{\partial t}(\rho u_i)+\frac{\partial}{\partial x_j}(\rho u_i u_j)=-\frac{\partial p}{\partial x_i}+\frac{\partial}{\partial x_j}\left[\mu\left(\frac{\partial u_i}{\partial x_j}+\frac{\partial u_j}{\partial x_i}\right)\right]+\frac{\partial}{\partial x_j}\left(-\rho\overline{u_i u_j}\right)$	(3)
LES model	$\frac{\partial\overline{u_i}}{\partial t}+\frac{\partial\left(\overline{u_i u_j}\right)}{\partial x_j}=-\frac{1}{\rho}\frac{\partial\overline{p}}{\partial x_i}+\nu\frac{\partial^2\overline{u_i}}{\partial x_j\partial x_j}-\frac{\partial\tau_{ij}^{sgs}}{\partial x_j}$	(4)
RSM model	$\frac{\partial}{\partial t}\left(\rho\overline{u_i'u_j'}\right)+\frac{\partial}{\partial x_k}\left(\rho u_k\overline{u_i'u_j'}\right)=D_{ij}+P_{ij}+\Phi_{ij}+\epsilon_{ij}$	(5)

In the equation, $\overline{u}_i, \overline{u}_j$denotes the filtered velocity component, $\overline{\mathrm{p}}$ denotes the filtered pressure, ρ denotes the bulk density, ν denotes the kinematic viscosity of the fluid, τ_{ij}^{sgs}denotes the sublattice scale stress$\tau_{ij^{sgs}}-\frac{1}{3}\tau_{kk}^{sgs}\delta_{ij}=-2\nu_t\overline{S}_{ij}$, ν_t denotes the sublattice eddy viscosity coefficient, and $\overline{\mathrm{S}}_{\mathrm{ij}}$ denotes the

filtered strain rate tensor; D_{ij} denotes the diffusion term $D_{ij}=\frac{\partial}{\partial x_k}\left(\mu\frac{\partial u_i'u_j'}{\partial x_k}\right)$, P_{ij} denotes the generation term $P_{ij}=-\rho\left(\overline{u_i'u_k'}\frac{\partial U_j}{\partial x_k}+\overline{u_j'u_k'}\frac{\partial U_i}{\partial x_k}\right)$, Φ_{ij} denotes the pressure-strain term $\Phi_{ij}=\overline{p^i\left(\frac{\partial u_i'}{\partial x_j}+\frac{\partial u_j'}{\partial x_i}\right)}$, and ϵ_{ij} denotes the viscous dissipation term $\epsilon_{ij}=\frac{2}{3}\rho\epsilon\delta_{ij}$.

The equations for translational and rotational motion of particles at time t are given by Eqs. 5-6.

$$m_{p,i}\frac{du_{p,i}}{dt}=F_{p-g,i}+\sum_{j=1}^{k_i}(F_{c,ij}+F_{d,ij})+m_{p,i}g \tag{6}$$

$$I_{p,i}\frac{d\omega_{p,i}}{dt}=\sum_{j=1}^{k_i}(T_{ij}+M_{ij}) \tag{7}$$

where $\mathbf{m_{p,i}}$, $I_{p,i}$, $u_{p,i}$, and $\omega_{p,i}$ denote respectively the mass, moment of inertia, translational velocity, and rotational velocity of i. The forces acting upon the solid include the liquid-solid interaction force $F_{p-g,i}$, the forces between particles i and i comprising the contact force $F_{c,ij}$ and viscous damping force $m_{p,ig}$, as well as the gravitational force $m_{p,ig}$. The force experienced by particle i is the sum of the forces exerted by all particles with which it is in contact. When the forces between particles act upon the contact point between particles i and i, a torque T_{ij} is generated. M_{ij} represents the rolling friction torque opposing the rotational direction of the first particle.

Besides, for the interaction forces between particles and fluid, this paper employs the Wen & Yu drag (Wen, 1966) calculation model, whose formula is as follows:

$$F_d=\beta\epsilon^{-2.65}(u_w-v_p) \tag{8}$$

$$\beta=\frac{3}{4}C_d\frac{\epsilon|u_w-v_p|}{d_p} \tag{9}$$

$$C_d=\frac{24}{Re_P}(1+0.15Re_P^{0.687}) \tag{10}$$

$$Re_p=\frac{2\epsilon\rho_w r_p|u_w-v_p|}{\mu_w} \tag{11}$$

In the equation: C_d is the drag coefficient associated with the particle Reynolds number.

This simulation employs the VOF multiphase flow model with the LES turbulence model. The SIMPLEC pressure-velocity coupling algorithm is utilized, and the pressure equation adopts the PRESTO discretization scheme. The momentum equation is formulated as a second-order upwind scheme, with an inlet velocity of 5 m/s.

The average particle size of coal entering the TPHS is 0.2 mm. With a density of approximately 1.4 g/cm³, the particles are assumed to be independent and spherical. The particle phase time step is set to 8×10^{-7} s. Detailed CFD-EDM parameter settings are shown in Table 2.

Table. 3. CFD-DEM Parameter Settings

Material phase	Parameters	Value
Liquid phase	Multiphase flow model	VOF
	Turbulence model	LES
	Fluid initial velocity	5m/s
	Time step	8×10^{-5}s
	Fluid density (ρ)	1000 kg·m^{-3}
	Poisson ratio (ν)	0.2
	Shear modulus (G)	1×10^{6}pa
Particle phase	Particle Density (ρ)	1400 kg·m^{-3}
	Time step	8×10^{-7}s
	Particle initial velocity	5m/s
	Collision recovery coefficient	0.53
	Static friction coefficient	0.44
	Coefficient of rolling friction	0.034

3. Results and discussion

3.1. Model validation

This study employs two turbulence models: the Reynolds Stress Model (RSM) and Large Eddy Simulation (LES). To determine the most suitable turbulence model, the velocity field obtained from PIV experiments was compared with Fluent simulation results at three radial positions within the MHS (R = 18.75, 56.25, 75). Fig. 4 displays the comparison of velocity contour lines, with the upper panel representing the radial velocity (U) and the lower panel depicting the tangential velocity (V).

Both simulation results show similar flow patterns to the PIV measurements, confirming that the main swirling structure and shear layers were well captured. The LES model agrees more closely with experimental data, particularly in the high-velocity and near-wall regions, where it better resolves local gradients and small-scale vortices. The RSM model tends to underestimate the velocity magnitude in the recirculation region and slightly shifts the velocity peak inward at larger radii.

In summary, the LES model provides better consistency with the PIV results in both velocity magnitude and distribution, demonstrating higher accuracy in predicting the complex flow within the MHS.

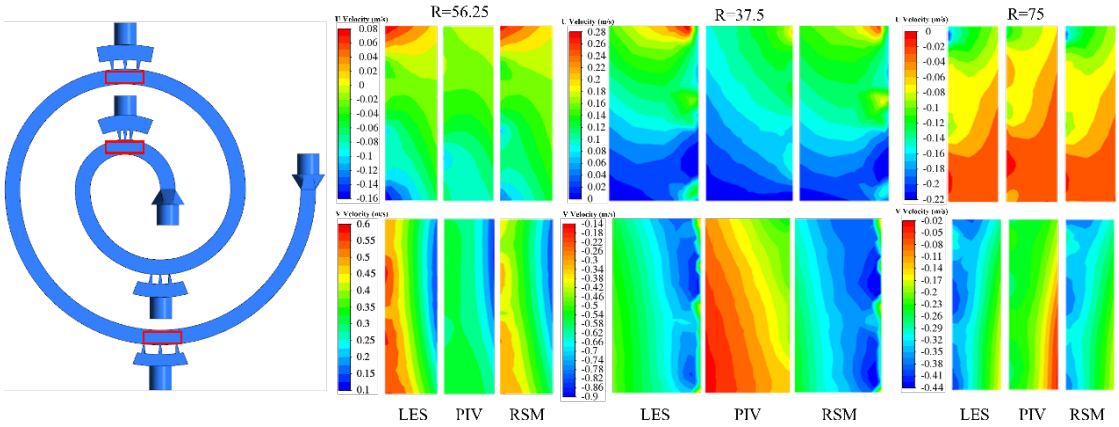

Fig. 4. Comparison of PIV, LES, and RSM velocity contours of U and V at different radial positions

3.2. Characteristics of fluid flow

Fig. 5 illustrates the overall velocity distribution inside the MHS at an inlet velocity of 5 m/s. Noticeable differences in velocity magnitude are observed at different rotation radii. The overall trend indicates that the flow velocity gradually decreases with increasing rotation radius. The second, third, and fourth sections exhibit similar flow characteristics, where the velocity field remains relatively stable without obvious vortex structures. In contrast, the outer region of the swirling channel shows slightly higher velocities than the inner region. Moreover, compared with the latter two sections, the flow field in the first stage—with the smallest rotation radius—contains several unstable flow zones, and its instability is more pronounced. This occurs because the fluid interacts strongly with the wall upon entering the swirling screening pipe, resulting in higher turbulence intensity. As the flow develops downstream, the wall influence weakens, and the velocity field becomes progressively more stable.

Fig. 6 shows the velocity vector distribution characteristics of the first (a) and second (b) stages of the MHS, with the right side displaying a magnified region of the swirl tube. Overall, after entering the swirl tube, the fluid forms a distinct rotating flow structure due to curvature and centrifugal forces. Within the enlarged right-hand region of the first section's flow field (Fig. a), vector directions are disordered. The fluid velocities on both sides are higher than that at the center, with small vortices present locally, indicating high turbulence intensity and significant energy dissipation in this area. As the fluid flow's along the pipe, the velocity gradually decreases. Although the velocity distribution remains uneven, the flow field progressively stabilizes. In the second flow segment, the fluid undergoes a distinct acceleration phase before reaching the screen openings. Upon entering the screen openings, the flow velocity markedly decreases. Overall, the velocity distribution becomes relatively uniform, and the turbulence intensity significantly weakens. This indicates that after energy dissipation and flow

reorganization in the first segment, the internal flow state in the second segment stabilizes, leading to a steadier flow pattern in the subsequent cyclone screening section.

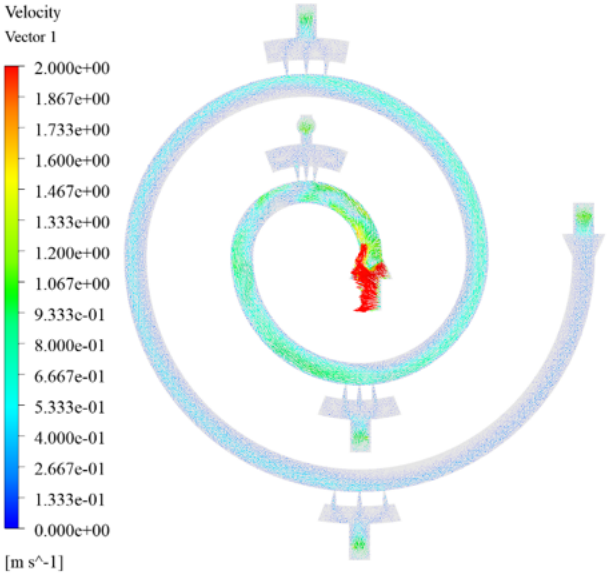

Fig. 5. Velocity vector diagram of multi-stage vortex screening structure

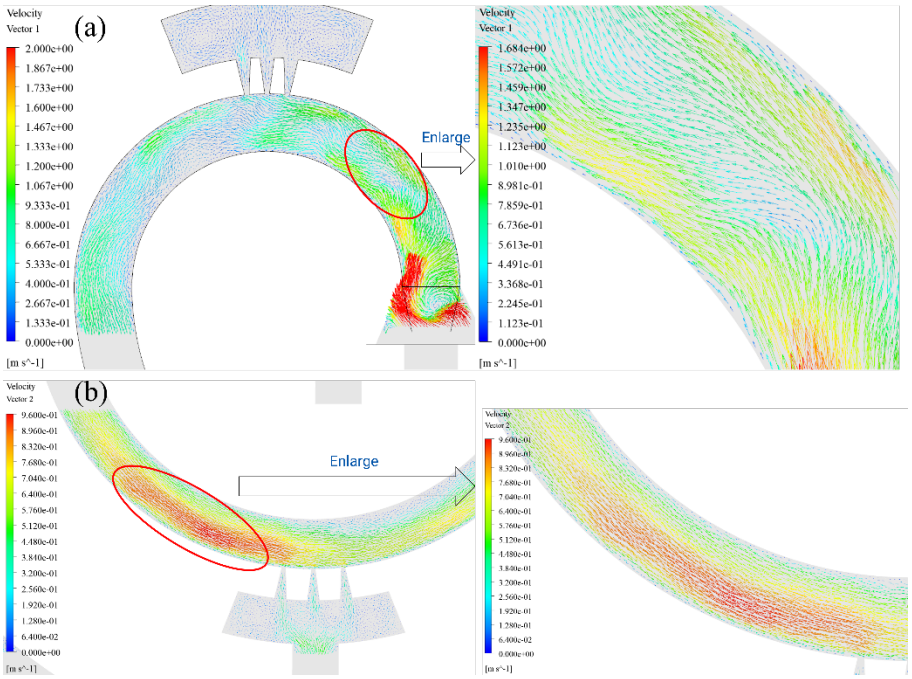

Fig. 6. Velocity vector diagram of multi-stage vortex screening structure

Fig. 7 shows the velocity vector diagrams at the inlet of the screen slots for the first section (a) and second section (b) of the cyclone screening structure. Regarding the velocity distribution, the fluid velocity distribution in the first section (a) is uneven, with chaotic vector directions. Compared to the first section (a), the fluid velocity distribution in the second section (b) is more uniform, with vector directions tending to align. A distinct velocity gradient is observed, where the fluid velocity upstream of the screen aperture is higher than downstream, and the velocity on the outer side of the vortex tube is higher than on the inner side. This indicates that the turbulence intensity at the inlet of the first section (a) is relatively high, causing accelerated fluid velocities in certain areas. This turbulence contributes to increased fluid kinetic energy. Both the first section (a) and second section (b) exhibit significant velocity

reductions at their inlet screen openings, indicating substantial kinetic energy dissipation as the fluid passes through the screen. The Energy dissipation is clearly pronounced in the first section.

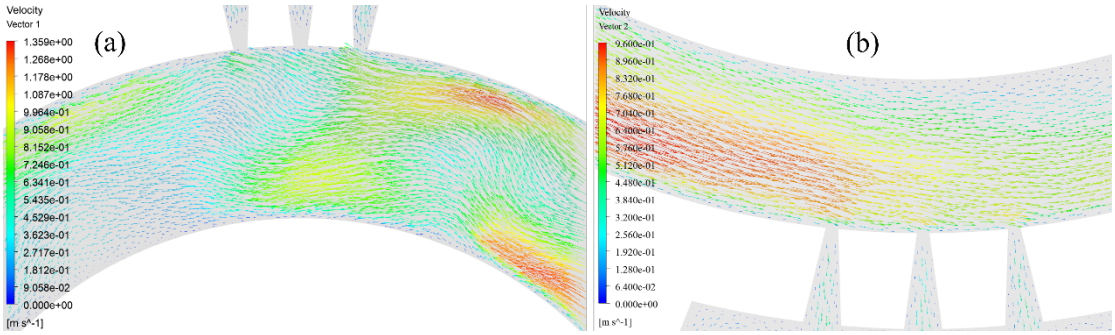

Fig. 7. Velocity vector diagram of the main flow channel at the screen inlet

To further analyze the internal flow field characteristics of the cyclonic screening process and investigate the velocity distribution within the screen slots, Fig. 7 displays the velocity vector distributions within the first (a) and second (b) screen slots of a MHS. From the flow field variation patterns, it is evident that the non-uniform velocity distribution within the screen slots generates significant velocity gradients. Localized micro-vortex phenomena are present, with the uneven velocity distribution primarily concentrated within the first screen gap where the fluid enters. In subsequent screen gaps, the flow field tends toward stability, and the velocity direction becomes more uniform. This indicates that turbulence and vortices are mainly confined to the first screen gap, resulting in greater velocity fluctuations within it. To more intuitively display the velocity changes within the screen gap, an observation point was established inside the gap, as shown in Fig. 8.

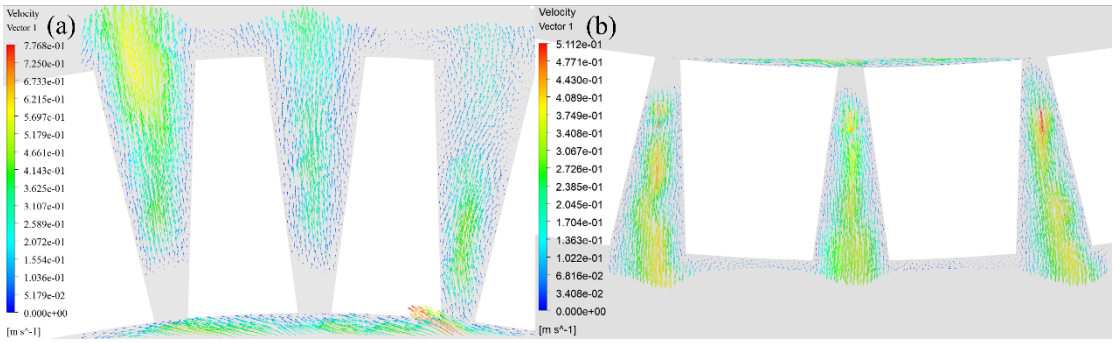

Fig. 8. Velocity vector diagram of the permeating zone

Fig. 9 illustrates the velocity distribution changes within the first and second screen gaps of the MHS model, with the red solid line indicating the observation line position. Overall, the velocity variation patterns along the Y-axis exhibit high similarity across different screen gaps. Approximately 1 mm after the fluid leaves the main flow channel and enters the screen gap, the velocity rapidly increases to a peak before initiating a decline. Within the first screen gap, the velocity gradient at the first gap location is significantly greater than at the other two gaps, indicating more pronounced flow acceleration at this position. After each screen gap reaches its first velocity peak, the velocity generally decreases with increasing Y-axis coordinates but subsequently exhibits some degree of fluctuation. In contrast, the second screen gap exhibits a pronounced change in velocity gradient over a short distance following its peak velocity, after which the velocity gradually stabilizes and ultimately converges across different screen gaps. Within the first section, the velocity at the third screen gap consistently remains higher than at the others. This pattern indicates that upon entering the screen gap, the fluid experiences enhanced kinetic energy due to swirling and shear effects, significantly intensifying the flow and forming a velocity peak at approximately 1 mm. Subsequently, the combined effects of turbulence and localized vortices within the screen gaps generate various forms of velocity fluctuations. As the fluid travels further through the gaps, turbulence gradually diminishes, the flow stabilizes, and velocities across all screen gaps ultimately converge.

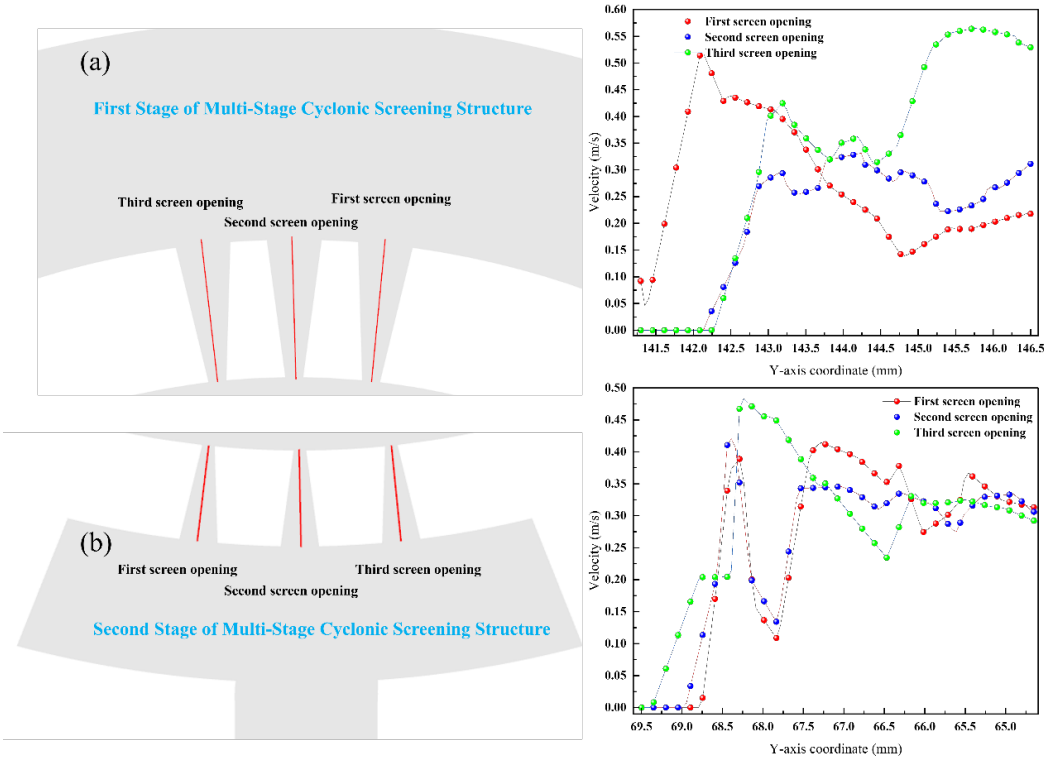

Fig 9 Speed variation diagram of the screening area (a) First stage of MHS, (b) Second stage of MHS

Fig. 10 shows the ratio of radial velocity to tangential velocity at the four rotational radii within the screen aperture. It can be observed that, except at the third rotational radius R=56.25mm where the tangential velocity consistently exceeds the radial velocity, radial velocity dominates over tangential velocity across most of the screen gap region for the other rotational radii. At the rotational radius R=75mm, the radial velocity at X=86mm is nine times the tangential velocity, and throughout the subsequent region, radial velocity remains at least double that of tangential velocity. Analysis indicates particles readily pass through the screen in this zone. At the R=56.25mm rotational radius, the tangential velocity consistently dominates within the screen aperture zone, indicating particles are unlikely to pass through at this point. At the R=37.5mm aperture zone, although radial velocity exceeds tangential velocity across a significant portion, radial velocity remains the primary force. The substantial influence of tangential velocity means particles have a probability of passing through at this location. At X=102 within the R=18.75mm screen gap region, the radial velocity substantially exceeds the tangential velocity. However, upon entering the screen gap zone, the ratio of radial to tangential velocity rapidly diminishes. At X=99, the magnitudes of radial and tangential velocities become comparable. This indicates favourable conditions for particle penetration upon initial entry into the screen gap region, but penetration efficiency diminishes after travelling a certain distance within the gap zone.

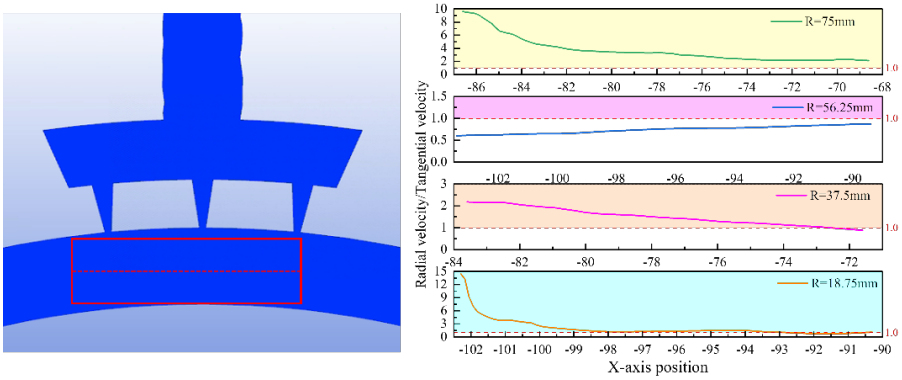

Fig 10 Comparison diagram of radial and tangential velocities at the observation line of the screen slit in a MHS

3.3. Feature of particle motion

3.3.1. Particle sieving process

To further analyses the specific motion characteristics of the particle sieving process, a section of the cyclone screening structure was selected to investigate particle movement. The local coupled simulation model is shown in Fig. 11, where the green region indicates the location of the particle factory and inlet.

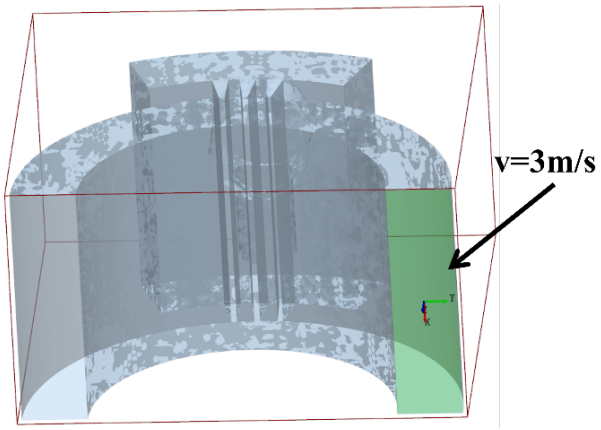

Fig. 11. Partially coupled simulation model

To ensure consistency in simulation results, all parameters except the model and inlet velocity were identical to those used in the overall simulation. The velocity distributions over time, as shown in Fig. 11, correspond to particle generation, prior to particle sieve penetration, during and after particle sieve penetration, and after particle sieve penetration.

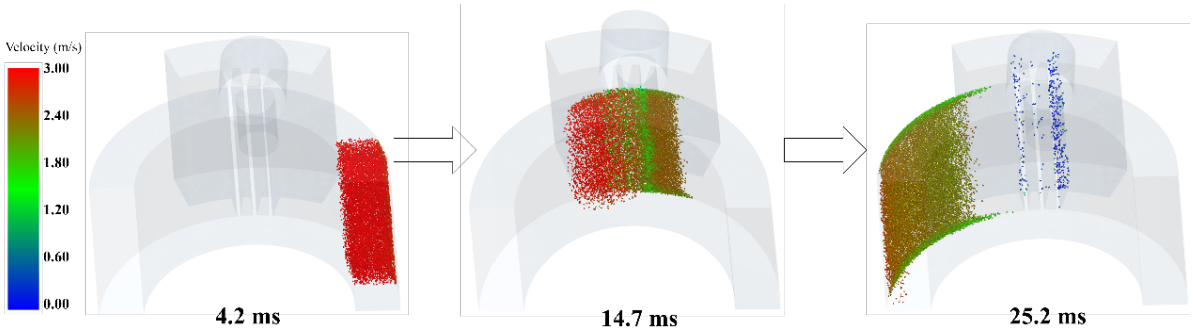

Fig. 12. Particle distribution diagram of the screening process in a cyclonic screening

At t=4.2ms, particles are largely formed, with all particles moving at a velocity of 3m/s. During this phase, particle motion is governed by the combined effects of gravitational force, pressure gradient force, and drag force. As particle velocity matches the fluid velocity, the influence of drag force on particle movement is negligible. Simultaneously, as particles approach uniform linear motion, the additional mass force and Basset force become negligible. Consequently, particles move with the fluid until colliding with the geometric structure's wall surface.

At t=14.7ms, particles collide with the geometric wall surface. Particles in the near-wall region experience a significant reduction in velocity due to collision and friction. During this phase, the particle primarily experiences stresses from particle-wall collisions and particle-particle collisions. As longitudinal forces exerted on the particle have negligible influence on the sieve-passing process, forces perpendicular to the direction of relative motion—such as lift, Magnus force, and Saffman force—are disregarded. The increased relative slip velocity between the decelerating particle and the fluid amplifies the impact of drag and inertial forces on its motion.

At t=25.2ms, particles commence the sieve penetration process. During this phase, numerous particles pass through the screen aperture, exhibiting marked deceleration at the aperture entrance. Particles already within the aperture form a low-velocity stream on the left side of the aperture. Analysis

of the flow field at the aperture reveals that vortices within the aperture influence particle motion. Particles move with the fluid vortices, where drag exerts a significant effect, substantially reducing particle velocity.

3.3.2. Particle sieve-passing trajectory

Fig. 12 illustrates the distribution characteristics of particle groups over time within a single-stage cyclone screening structure. The particle distribution reveals that the highest number of particles pass through the first screen opening, accounting for approximately 50% of the total passing particles. Regarding particle velocity changes, the overall velocity of particles before passing through the screen is essentially consistent with their velocity upon entering the cyclone screening structure. After passing through the screen, the velocities of most particles decrease significantly, with only a small number maintaining their initial velocity. Further observation of the screening behavior at the screen slots reveals that although the first slot allows the highest number of particles to pass through, its screening process duration is relatively longer. Calculations of the sieve passage time indicate that the first sieve slot took approximately 35 ms to pass through, while the third slot took about 15 ms. This suggests that fluid interactions within the first sieve slot significantly influence the particle sieve passage process, leading to prolonged passage times. To further investigate particle motion characteristics within a single-stage cyclone sieve structure, the trajectories of different particles within the sieve slots were tracked and analyzed, as shown in Fig. 13.

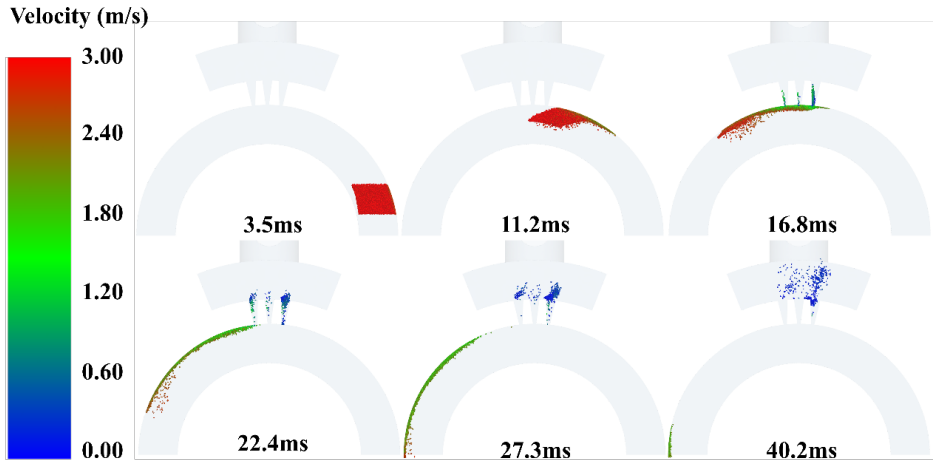

Fig. 13. Spatial motion characteristics of particle clusters in vortex screening structures

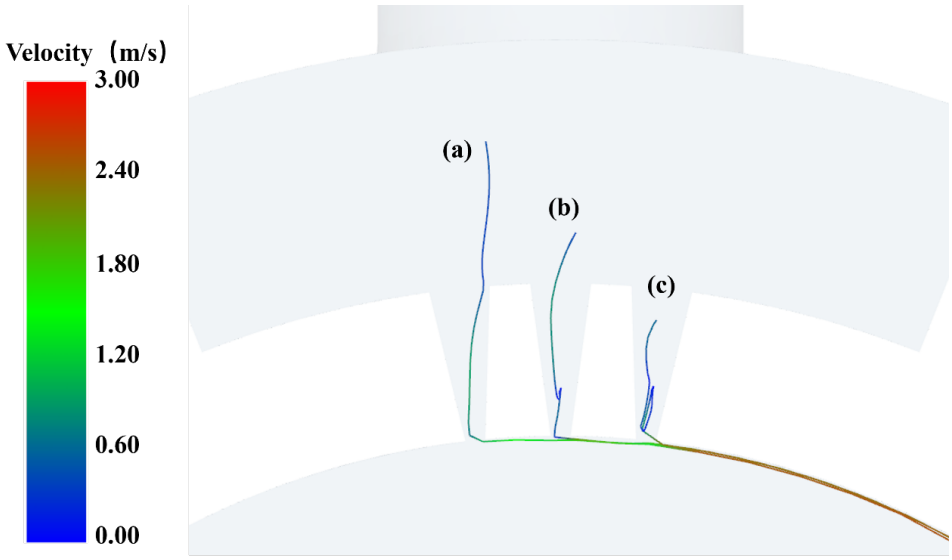

Fig. 14. Particle sieve passage trajectory diagram

Analysis of Fig. 13 reveals that particles passing through different screen apertures exhibit distinct motion characteristics. Particles within the right-hand aperture demonstrate markedly longer dwell times compared to those in the other two apertures. To illustrate particle motion more clearly, we selected the trajectories of the three particles (a), (b) and (c) that remained in each sieve aperture for the longest duration., as depicted in Fig. 14.

Analysis of the trajectories of the three particles in Fig. 14 reveals that in (a), particles are minimally affected by the vortex in the screen gap region, experiencing only a slight velocity deflection before exiting the gap. In (b), particles are entrained by the vortex, undergoing a brief retention period before escaping the vortex zone and passing through the screen. In (c), particles are significantly affected by the vortex selection mechanism, failing to pass through the screen for an extended period and even being drawn back into the main flow channel.

4. Conclusions

This study employs an LES model to investigate the internal flow distribution patterns within a swirl screening structure, thereby determining the fluid motion characteristics at the screen apertures. Building upon this, a CFD-DEM coupled simulation analyses the motion characteristics and patterns of particles during the screening process. The conclusions drawn are as follows:

(1) Significant turbulence is observed in the inlet region of the first flow channel section. This region exhibits high energy dissipation and flow instability characteristics; Multiple irregularly distributed vortex structures were observed within the main flow channel. Small-scale vortices and fluid recirculation phenomena were present in the central region of the screen aperture, with vortices exacerbating energy dissipation.

(2) At a rotational radius of R=75mm, radial velocities within the screen aperture region exceeded tangential velocities by more than double, resulting in significant particle screening efficiency in this zone; In the R=56.25mm screen gap region, tangential velocity forces dominate, resulting in poor particle screening efficiency; screening feasibility exists in the R=37.5mm screen gap region; fluid screening is pronounced immediately upon entering the R=18.75mm screen gap region, but screening efficiency deteriorates in subsequent zones.

(3) Prior to contacting the wall, particles maintain velocities close to the fluid flow while moving within the pipeline. Upon impact with the pipe wall, particle velocity decreases under drag force. Once particles enter the screen, vortices within the screen aperture influence particle motion, severely affecting particle velocity and screening efficiency.

(4) By comparing the trajectories of the three particles that remained within the screen slots for the longest duration, it is evident that a strong vortex affecting particle screening exists within the right-hand slot. Although vortices are present within the other slots, their impact on particle screening is relatively minor.

Acknowledgments

Natural Science Research Projeet of Anhui Educational Committee (2024AH050339); National key research and development Program of China (2023YFC3904004); Anhui Province Coal Clean Processing and Carbon Reduction Engineering Research Center Foundation (CCCE-2023001; CCCE-2024004); The University Synergy Innovation Program of Anhui Province (GXXT-2023-104).

References

AL KAYED QUTEISHAT, M. 2020. *Hydrocyclone flow characteristics and measurements*. Flow Measurement and Instrumentation. 73.

BING, L., LUNCAO, L., HUAJIAN, W., ZHENJIANG, Z., YAOGUANG, Q. 2020. *Numerical simulation and experimental study on internal and external characteristics of novel Hydrocyclones*. Heat and Mass Transfer. 56. 1875-1887.

CHEN, J., SHENG, L., WANG, C., ZHANG, Y. 2016. *Desliming performance of the three-product cyclone classification screen*. Journal of China University of Mining &, Technology. 45. 807-813

CHU, K W., CHEN, J., WANG, B., YU, A B., VINCE, A., BARNETT, G D., BARNETT, P J. 2017. *Understand solids loading effects in a dense medium cyclone: Effect of particle size by a CFD-DEM method*. Powder Technology. 320. 594-609.

EL-EMAM, M A., ZHOU, L., SHI, W., HAN, C., BAI, L., AGARWAL, R. 2021. Theories and Applications of CFD–DEM Coupling Approach for Granular Flow: A Review. Archives of Computational Methods in Engineering. 28. 4979-5020.

ESGANDARI, B., GOLSHAN, S., ZARGHAMI, R., SOTUDEH-GHAREBAGH, R., CHAOUKI, J. 2021. CFD-DEM analysis of the spouted fluidized bed with non-spherical particles. The Canadian Journal of Chemical Engineering. 99. 2303-2319

FULCHINI, F., GHADIRI, M., BORISSOVA, A., AMBLARD, B., BERTHOLIN, S., CLOUPET, A., YAZDANPANAH, M. 2019. Development of a methodology for predicting particle attrition in a cyclone by CFD-DEM. Powder Technology. 357. 21-32.

GAO, Y., PEI, X., CAO, G., YU, J., ZHAO, X., LI, F. 2023. *Effect of collision of particles on migration behaviour in hydrocyclone.* Journal of Physics: Conference Series. 2441.

HOU, D., ZHAO, Q., CUI, B., WEI, D., SONG, Z., FENG, Y. 2022. *Geometrical configuration of hydrocyclone for improving the separation performance*. Advanced Powder Technology. 33.

JI, L., PAUL, P., SHANBHAG, B K., DIXON, I., KUANG, S., HE, L. 2023. *Emerging application of hydrocyclone in biotechnology and food processing*. Separation and Purification Technology. 309. 122992.

JUNG, K J., HWANG, I-J., KIM, Y-J. 2019. *Effect of inner wall configurations on the separation efficiency of hydrocyclone*. Journal of Mechanical Science and Technology. 33. 5277-5283.

KOPPARTHY, S., MANSOUR, M., JANIGA, G., THéVENIN, D. 2020. Numerical investigations of turbulent single-phase and two-phase flows in a diffuser. International Journal of Multiphase Flow. 130. 103333.

KUANG, S., ZHOU, M., YU, A. 2020. CFD-DEM modelling and simulation of pneumatic conveying: A review. Powder Technology. 365. 186-207.

ZHANG, D-M., GAO, C-P., YIN, Z-Y. 2019. CFD-DEM modeling of seepage erosion around shield tunnels. Tunnelling and Underground Space Technology. 83. 60-72

KURUNERU, S T W., MARECHAL, E., DELIGANT, M., KHELLADI, S., RAVELET, F., SAHA, S C., SAURET, E., GU, Y. 2018. *A Comparative Study of Mixed Resolved–Unresolved CFD-DEM and Unresolved CFD-DEM Methods for the Solution of Particle-Laden Liquid Flows.* Archives of Computational Methods in Engineering. 26. 1239-1254.

LI, F., LIU, P., YANG, X., ZHANG, Y., ZHAO, Y. 2020. *Effects of inlet concentration on the hydrocyclone separation performance with different inlet velocity*. Powder Technology. 375. 337-351.

Li, P., SHENG, L., CHEN, J., ZHAO, X. 2011. *Technical characteristies and application of three-product classifying cyclones.* Mining & Processing Equipment. 39.1001-3954.

LI, Y., LIU, C., ZHANG, T., LI, D., ZHENG, L. 2018. *Experimental and numerical study of a hydrocyclone with the modification of geometrical structure*. The Canadian Journal of Chemical Engineering. 96. 2638-2649.

MISIULIA, D., LIDéN, G., ANTONYUK, S. 2021. Evolution of Turbulent Swirling Flow in a Small-Scale Cyclone with Increasing Flow Rate: A LES Study. Flow, Turbulence and Combustion. 107. 575-608.

MULBAH, C., KANG, C., MAO, N., ZHANG, W., SHAIKH, A R., TENG, S. 2022. *A review of VOF methods for simulating bubble dynamics.* Progress in Nuclear Energy. 154.

PADHI, M., VAKAMALLA, T R., MANGADODDY, N. 2022. *Iron ore slimes beneficiation using optimised hydrocyclone operation*. Chemosphere. 301. 134513.

ROCHA, C A O., ULLMANN, G., SILVA, D O., VIEIRA, L G M. 2020. *Effect of changes in the feed duct on hydrocyclone performance*. Powder Technology. 374. 283-289.

SALVADOR, F F., BARROZO, M A S., VIEIRA, L G M. 2016. *Effect of a Cylindrical Permeable Wall on the Performance of Hydrocyclones*. Chemical Engineering & Technology. 39. 1015-1022.

VAKAMALLA, T R., MANGADODDY, N. 2017. Numerical simulation of industrial hydrocyclones performance: Role of turbulence modelling. Separation and Purification Technology. 176. 23-39.

VYSYARAJU, R., PUKKELLA, A K., SUBRAMANIAN, S. 2022. Computational investigation of a novel hydrocyclone for fines bypass reduction. Powder Technology. 395. 501-515.

WANG, C., CHEN, J., SHEN, L., GE, L. 2020. *Study of flow behaviour in a three products hydrocyclone screen: numerical simulation and experimental validation*.

WEN, C-Y. 1966. Mechanics of Fluidization.

XIONG, Z., XU, J., LIU, C. 2023. Interaction effects of inlet velocity and apex diameter on the separation performance of two-stage cone hydrocyclones. Powder Technology. 422. 118446.

YU, J., WANG, S., KONG, D., LUO, K., FAN, J. 2023. Coal-fueled chemical looping gasification: A CFD-DEM study. Fuel. 345. 128119.

YU, J-F., FU, J., CHENG, H., CUI, Z. 2017. *Recycling of rare earth particle by mini-hydrocyclones. Waste Management.* 61. 362-371.

ZHANG, P., SHENG, L., CHEN, J., ZHAO, X. 2011. *Technical characteristics and application of three-product classifying cyclones.* 39. 92-95.

ZHANG, Y., LIU, P., GE, J., YANG, X., YANG, M., JIANG, L. 2021. Simulation analysis on the separation performance of spiral inlet hydrocyclone. *International Journal of Coal Preparation and Utilization.* 41. 474-490.